Results in Engineering 13 (2022) 100364

Contents lists available at ScienceDirect

Results in Engineering

journal homepage: www.sciencedirect.com/journal/results-in-engineering

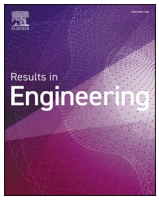

Finite element simulation on the convective double diffusive water-based copper oxide nanofluid flow in a square cavity having vertical wavy surfaces in presence of hydro-magnetic field

M.J. Uddin [a,*], S.K. Rasel [b,d], Jimoh K. Adewole [a], Khamis S. Al Kalbani [c]

[a] Department of Engineering, International Maritime College Oman, Sohar, Oman
[b] Department of Mathematics, Rangpur Polytechnic Institute, Rangpur, 5400, Bangladesh
[c] Faculty of Education and Arts, Sohar University, Sohar, Oman
[d] General Educational Development, Faculty of Science and Information Technology, Daffodil International University, Dhaka, 1207, Bangladesh

ARTICLE INFO

Keywords:
Nanofluid
Nanoparticle
Hydromagnetic field
Heat transfer
Vertical wavy surfaces and
Finite element method

ABSTRACT

We explored natural convection of copper oxide-water nanofluid flow within a square domain having two wavy vertical surfaces in existence of the hydro-magnetic field using non-uniform dynamic model. Two vertical surfaces on the left and right are regarded as connecting outlets through which heat can pass and considered as the colder walls, the bottom surface is regarded as a uniform heat source, and the upper boundary line is regarded as an insulating surface through which heat cannot pass. The Galerkin's extension in the finite element analysis has been incorporated to design, transform, and solve the nanofluid equations. The results reveal that when the thermal Rayleigh number upturns, the amplitude of the velocity, streamlining, isotherms efficacy, and uniformity of the isoconcentration labeling increase for a nanofluid with reduced nanoparticle volume percentage. As the magnetic pitch intensifies, the flow strength drops, and effective flow occurs in the vertical magnetic field. Flow convolution develops as more waves are formed on a vertical surface. The average heat transmission rose by 158% as the Rayleigh number grew from 10^4 to 10^6. The mean heat transmission increases by 10.18% when the nanoparticle volume segment is increased from 0.025 to 0.05. The heat transmission rate is higher on the vessel's non-wave vertical surface. Heat transfer is reduced by 16.98% when the wave number is augmented to 2 and increased by 3.62% when the wave number is risen from 2 to 4.

1. Introduction

Recently, extensive interest has been given in the field of nanofluids flow and the increase of heat transfer using nanofluids. The comprehensive application of hybrid convective heat transport in different craters is used in engineering arrangements, such as heat modifiers, solar energy gleaners, electronic equipment for refrigerating, chemical treating apparatus, twofold-glassed windows, nuclear reactor cooling, and diet industry. Earlier, some fluids were used by industry for convective heat transmission purposes, but now they are less important due to their low thermal conductivity. The applications of nanofluids and its potentialities are well analyzed in the literature ([1–7], and [8]). Today, to meet industrial needs, the industry is considering the use of nanofluids with high thermal conductivity. In addition, finding an alternative solution that can transfer a lot of heat is crucial. Nanofluids are a special kind of high convective element comprising of the base fluid (like water) and nanomaterials (like Al_2O_3, Cu, CuO, and TiO_2) that have high thermal conductivity. Although many studies on the use of natural convection fluids to enhance heat transfer have been published in the literature, most studies have shown that the expected heat transfer results related to heat transfer parameters have failed. The study of mixed convection heat transfer in nanofluid flow may be an important requirement to meet industrial needs. Based on the variation of parametric values and understanding of the flow mechanism of nanofluids, many studies are conducted on nanofluidic convective heat transfer in different types of geometries. A complete assessment of various types of nanofluids including substantial impacts of parameters on heat transport augmentations as well as to identify the changes of heat transport by applying analytical or mathematical modellings are available in the literature [9].

* Corresponding author.
E-mail address: jashimuddin@imco.edu.om (M.J. Uddin).

https://doi.org/10.1016/j.rineng.2022.100364
Received 22 December 2021; Received in revised form 29 January 2022; Accepted 4 February 2022
Available online 8 February 2022

The analysis of the nanofluid phenomenon and parameter expression and influence in the optimized object design has become a key factor in understanding the enhancement of heat transfer in real-life applications [10]. Intricate shapes, such as various enclosures with undulating boundaries, require extensive and exclusive analysis because of the computational need. The flow analysis and heat transfer characteristics are found in different nanofluid-filled undulating walled craters using usual fluids [11–14]. The mean Nusselt number rises in concordance with the Richardson number as the volume proportion of nanoparticles rises. Among hydro-centered alumina, copper oxide, and TiO_2 nanofluids, the best heat transport performance is driven by CuO–H_2O nanofluid. By appropriately changing the geometric constraints of the wave-shaped surface, the average Nusselt number can be optimized, which plays a crucial part in enhancing the rate of heat transmission of the mixed convective nanofluid flow [15]. The literature provides many results on heat transfer with defined parameters for specific problems. In addition, the various viscosity and thermal conductivity models that define the effectiveness of nanofluids differ in various studies. On studying buoyancy driven natural heat transfer and flow fields of AlO_2–H_2O nanofluid inside the square shaped cavity having vertical sinusoidal side walls, Brinkman and Maiga's viscosity correlation models have found considerable differences on overall heat transport.

For the Rayleigh number, greater than 1000, the mean Nusselt expression intensified by the Brinkman technique but dropped by Maiga's method [16]. The influence of nanoparticle volume fraction, amplitude and wavelength on flow and heat transfer is of great significance for studying the usual heat upwelling and entropy production of hydro-alumina nanofluids in quadrangular cavities. As the parameters of the intended problem change, substantial results are found in the enhancement of mean Nusselt sum and complete entropy creation [17]. The heat transfer rate increased sharply as the thermal conductivity of the nanoparticles and the absorption rate of the medium increased, but it reduced when the porosity decreased. Significant effects of various parameters on heat transfer and flow have been observed, such as Darcy parameters, modified conductivity ratio of nanofluids, surface wave number, and absorption media of alumina-water nanofluids flowing in various cavities, with curling bottom heating wall and the inner solid cylinder [18]. Tang et al. [19] have examined the free convection in a crater with dual sinusoidal curvy walls using Ag-Water, CuO-Water, Al_2O_3-Water nanofluid. Their study shows that the Ag-Water nanofluid produces remarkable surface heat transfer coefficient in comparison to others. A similar study was conducted by Abdulkadhim et al. [20] taking Ag-water nanofluid filled wavy annular porous enclosure in concern. They exposed that the movement of the sinusoidal cylinder has considerable effects on the flow strength and the width of the permeable layer on the average heat transfer performance. A series of investigations [21–23] on heat transmission were performed using water-based copper nanofluid in an undulated square enclosure. Their results show that the augmentation of the wavy amplitudes and wavelengths deteriorate the mean Nusselt number, but a quite opposite behavior shows for the fixed Rayleigh number 10^4. The leaning angle and arrangement of the heat source have significant effects on the declination of heat transmission. The thermal transport operation is highly affected by the heat source locations, the angle of the enclosure, concentration of nanofluid, and the properties of porous medium. Additionally, the average entropy production uplifts because of an increase of the wave number, and the amplitude of the temperature dispersal along the heated wall. Sheremet et al. [24,25] performed algebraic investigation of free convection and unsolidified movement in porous wavy voids occupied with nanofluids in the presence of Brownian diffusion and thermophoresis. They found that changes in heat generator's size, Rayleigh and fluctuation numbers have a significant consequence to the stream and heat transmission rate. However, Nusselt number on both of the inner and outer boundaries is drastically augmented due to the spate of the deemed constraints of the study. The shape factor effects of buoyancy driven heat transmission mechanisms in a convectively heated four-sided enclosure with a rounded fence inside, copper-oxide-water nanofluid filled annular space can be a potential factor to enhance heat transfer. The larger the surface area, the higher the heat transfer. Hence, influence of the particle shape factor and the medium on the buoyancy-driven heat transfer mechanism in a partially heated rhombus shell, in which there is a circular barrier, and the annular space is filled with copper oxide-water nanofluid, which may be potential factors to enhance heat transfer [26]. Studies have shown that the rate of heat transmission is enhanced for the increment in Rayleigh number and reduced due to rise in volumetric concentration of the nanoparticles in the fluid. Also, platelet shape of nanoparticles exhibits the greater rate of heat transport. Gheynani et al. [27] examined the influences of the diameter of the carboxymethyl cellulose/CuO nanofluid inside a microtube and exposed that for the fixed Reynolds number, the convection heat transfer coefficient increases as nanoparticle diameter decreases. Ullah et al. [28] carried out examination of free convective flow of CuO–H_2O nanofluid inside the rectangular crater having wavy warmed walls, and the outcomes revealed that the temperature distribution and flow field become stronger owing to the increment of Rayleigh and wavelength number. Furthermore, it was observed that the rise of the nanoparticle size fraction improves the rate of heat generation. Patel et al. [29] observed the operation of usual convective heat transport and radiation thermal transfer in a partly warmed quadrangle fissure by means of air and aquatic based nanofluids. The analysis made remarkable comparisons using water and various hydromagnetic based alumina and silver nanofluids. For the cases of heat transfer compared to air, alumina nanofluid executes worthily well with a variation in radiation heat transfer of 60.8 and 53.19% while for convective heat transfer the variation detected was 98.4 and 97.8%, respectively. Since the concentration of these nanofluids is higher than that of air, it is difficult to achieve thermal stratification. A circular wavy heater as a source on nanofluid filled heat transfer object can lead a decisive part in the heat intensification and government of the convective flow characteristics [30].

Many diversified results have been observed in the literature on thermal transport enhancement via nanofluidic flow. The intention of the current investigation is to look over the intensification and alleviation of heat transmission rate for CuO–water nanofluid filled quadrangular enclosure holding leftward and rightward cosine corrugated sides. The fluid flow and heat transfer characteristics of the arrangement are examined through a 2D nonhomogeneous vibrant model. Two-sided wavy walled square shaped geometries have widespread applications in mechanical and power generation industries. Some heat exhausting and electric devices have undulated square void shaped devices. By scrutinizing heat carrying performance of various types of cavities, it is crucial to find an appropriate heat bearer device for engineering use. Accordingly, the observation of thermal dispersion and movement characteristics in a nanofluid-filled quadrangular container having leftward and rightward curly walls could be valuable in science and engineering. Uddin et al. [31] explored heat transfer amplification for diverse values of concentration, Rayleigh Number, undulation number and geometry inclinations. Many researchers also ignore the Brownian and thermophoretic characteristics and the molar concentration effect of nanofluids. In our analysis, these effects are considered. Many experiments can be found in the literature under various wave geometries. However, as far as we know, a method for uniformly heating the lowermost wall with adiabatic leftward and rightward wave boundaries in a quadrangular vessel filled with aquatic based CuO nanofluid using dynamic parameters has not been investigated yet. The special effects of vertical surface wavenumber, intensity and inclination of magnetic field, thermal Rayleigh number, particle volumetric fraction and particle diameter on the flow and thermal fields in terms of isotherms, streamlines, velocity magnitude contour and isoconcentrations and the heat transfer rate using Nusselt number are newly analyzed. The study of natural convection and conduction in a vertical wavefront square vessel heated by a uniform heater on the bottom wall is innovative.

2. Physical and mathematical modeling

A three dimensional and cross-section (2D) sketches are shown in Fig. 1. The lower wall of the square cavity works as a uniform source of heat for the entire system while the upper barrier is colder and is set at a constant temperature. Also, the leftward and rightward wavy walls are adiabatic. The length of the sides of the square is L and the wavy walls are formulated by the parametric equations as follows:

$$x = a[1 - \cos(2\pi k y)],\ 0 \le y \le L \tag{1}$$

$$x = [1 - a\{1 - \cos(2\pi k y)\}],\ 0 \le y \le L \tag{2}$$

here, x and y are the ordinates of the 2-D coordinates, the wall wave amplitude is a and the number of waves is k. We have considered the wavelength $a = 0.05$ and varies number of waves k. The fluid inside the enclosure is presumed to be CuO–water nanofluid. Various advantages of the use of copper oxide nanoparticles in the applications have attracted many scientists to conduct more and more studies on CuO–H_2O nanofluid. Copper oxide nanoparticles (CuO) are monoclinic, stable, nonflammable, magnetized and insoluble in water. Black colored copper oxide nanoparticles are available commercially for the application. The CuO-water nanofluid was prepared in-house from commercially available raw materials, and their nano-characterizations are also available in the literature. The higher thermal conductivity of the copper oxide-water nanofluid significantly emphasizes its potential application in heat transfer application.

To analyze the flow field and heat transfer, the nanofluid continuity, momentum, energy and concentration equations are employed (see Uddin et al. [31] and Uddin et al. [32]) and are abridged by dint of the succeeding assumptions:

(i) To obtain accuracy of the results, the conservation equations of nanofluids are formed taking the slip mechanisms into account.
(ii) Nanofluid as a special fluid having easily fluidizable nano-solids in the base fluid.
(iii) The nanofluid is Newtonian and the flow is a 2D incompressible, laminar, and time dependent.
(iv) The upper wall is kept at low temperature as heat passes through it and termed as $T = T_C$.
(v) Primarily, the nanofluid concentration C_C is low, but as time passes ($t > 0$), throughout the entire flow field, it's level is C_h ($C_h > C_C$).
(vi) The effects of Brownian diffusion, thermophoresis, and gravitational acceleration are involved.
(vii) No chemical reaction between base fluid and nanoparticles are maintained as well as no radioactive heat transport is considered in the system. The chemical reaction between the nanoparticle and the base fluid is neglected in the model because the activation energy of nanoparticles is not given in the mixture so that the chemical bonds of the particles can be broken. There is also no proper orientation among the nanoparticles are assumed so that chemical reaction can be measured. The mechanisms of chemical reactions between nanoparticles and the base fluid are important phenomena. The analyzing chemical reactions in a mathematical model will provide to predict the reactor performance for the system. This study can be helped to understand the food processing and design of the chemical processing equipment, temperature distribution, moisture over agricultural fields and formation and dispersion of fog.
(viii) The nano-solids and the base fluid are in thermal symmetry.
(ix) A uniform magnetic field $\mathbf{B} = (B_0 \cos\gamma,\ B_0 \sin\gamma,\ 0)$ where, B_o is the magnitude and the angle between magnetic field direction and positive x-axis is γ.

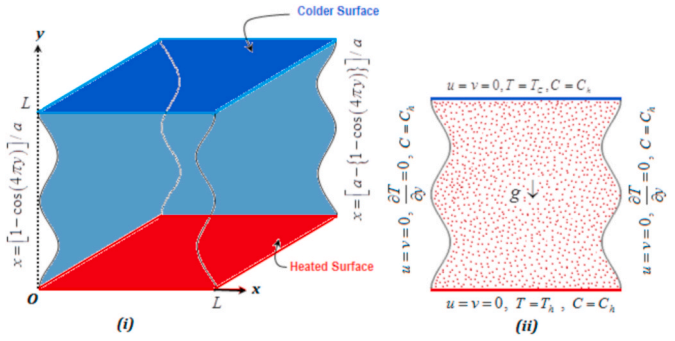

Fig. 1. The physical model of the enclosure. (i) 3D (ii) 2D.

Therefore, based on the abovementioned norms, the 2D unsteady dynamic conservation equations for nanofluids respectively in rectangular system of coordinates can be put down as follows:

Continuity Equation:

$$div\ \overline{u} = 0 \tag{3}$$

Momentum Equation:

$$\frac{\partial \overline{u}}{\partial t} + \overline{u}\cdot\nabla\overline{u} = -\frac{1}{\rho_{nf}}\nabla\overline{p} + \frac{\mu_{nf}}{\rho_{nf}}\nabla^2\overline{u} + \frac{F}{\rho_{nf}} + \frac{1}{\rho_{nf}}(\overline{J}_E \times \overline{B}) \tag{4}$$

Energy Equation:

$$\frac{\partial T}{\partial t} + \overline{u}\cdot\nabla T = \alpha_{nf}\nabla^2 T + \frac{D_B}{C}(\nabla C\cdot\nabla T) + \frac{D_T}{T}(\nabla T\cdot\nabla T) \tag{5}$$

Concentration Equation:

$$\frac{\partial C}{\partial t} + \overline{u}\cdot\nabla C = D_B\left(\nabla^2 C\right) + \frac{D_T}{T}(\nabla C\cdot\nabla T) + \frac{CD_T}{T}\left(\nabla^2 T\right) \tag{6}$$

$$F = \begin{cases} 0 & ,\ \text{along } x-\text{axis} \\ g\left((\rho\beta)_{nf}(T - T_c) + (\rho\beta^*)_{nf}(C - C_c)\right), & \text{along } y-\text{axis} \end{cases} \tag{7}$$

The details of the above governing equations of the current problem are well analyzed and described by Uddin et al. [31] and Uddin et al. [32]. As a result of the combined effect of the fluid velocities and imposed magnetic intensity, a force $(\overline{J}_E \times \overline{B})$, $\overline{J}_E = \sigma_{nf}(\overline{E} + \overline{u} \times \overline{B})$, called the Lorentz force is created, where, $\overline{u} = (u, v, 0)$ is the fluid velocity, $\overline{E}$ is the electric field, $\overline{B} = B_o(\cos(\gamma), \sin(\gamma), 0)$ is the magnetic field,σ_{nf} is the nanofluid's electric conductivity, and $\overline{x} = (x, y, 0)$. Since the surface is electrically nonconductive, the applied magnetic field and the Lorentz force create the following expressions (8) and (9) alongside the x and y-force equations [33].

$$\sigma_{nf}B_0^2[v\cos(\gamma) - u\sin(\gamma)]\sin(\gamma) \tag{8}$$

$$\sigma_{nf}B_0^2[u\sin(\gamma) - v\cos(\gamma)]\cos(\gamma) \tag{9}$$

Due to the uncertainty of the obtained results, it is hard to calculate the relation among the thermophysical properties of nanofluid. Though the viscosity of nanofluid is assessed by a standing relationship for a two-factor combination, a number of relationships of the thermophysical characteristics of nanofluids are found in the previous investigations [32]. The following correlations are used in the governing equations [24,25,27,28,30,34–39] and can be summarized as

$$\sigma_{nf} = \left[\frac{3\varphi(\sigma_p - \sigma_{bf})}{2(\sigma_{bf} + \sigma_p/2) + (\sigma_{bf} - \sigma_p)\varphi} + 1\right]\sigma_{bf} \tag{10}$$

$$\mu_{nf} = \frac{\mu_{bf}}{(1-\varphi)^{2.5}} \tag{11}$$

$$\rho_{nf} = \rho_{bf} + \varphi(\rho_p - \rho_{bf}) \tag{12}$$

$$(\rho c_p)_{nf} = \kappa_{nf}/\alpha_{nf} \tag{13}$$

$$\kappa_{nf} = \frac{\kappa_{bf}\left[(n-1)\kappa_{bf} + \kappa_p - (n-1)\varphi(\kappa_{bf} - \kappa_p)\right]}{\left[(n-1)\kappa_{bf} + \kappa_p + \varphi(\kappa_{bf} - \kappa_p)\right]} + \frac{\rho_p c_p \varphi}{2D_T^l}\sqrt{\frac{2k_B T_C D_T}{3\pi\mu_{nf} d_p}} \tag{14}$$

$$(\rho c_p)_{nf} = (\rho c_p)_{bf} + \varphi\left[(\rho c_p)_p - (\rho c_p)_{bf}\right] \tag{15}$$

$$(\rho\beta)_{nf} = (\rho\beta)_{bf} + \varphi\left[(\rho\beta)_p - (\rho\beta)_{bf}\right] \tag{16}$$

$$(\rho\beta^*)_{nf} = (\rho\beta^*)_{bf} + \varphi\left[(\rho\beta^*)_p - (\rho\beta^*)_{bf}\right] \tag{17}$$

$$D_B = \frac{k_B T_C}{3\pi\mu_{nf} d_p} \tag{18}$$

$$D_T = \frac{126\beta_{bf}}{1000}\frac{\mu_{nf}\kappa_{nf}}{\rho_{nf}\kappa_{bf}}\text{ƛ} \tag{19}$$

$$\text{ƛ} = -0.0002\mathrm{d_p} + 0.1537 \tag{20}$$

The numerical values of Equations. (10), (11), (12), (13), (14), (15), (16), (17), (18), (19) and (20) are attained via thermophysical characteristics of the nano-solids and regular base fluid displayed in Table 1.

In our stated model, the following primary and wall conditions are utilized.

$$At\ t = 0,\ (u,v) = (0,0),\ p = 0,\ C = C_C,\ T = T_C \tag{21}$$

At $t > 0$,

$$For\ x \in [0,L]\ y = 0\ .\ (u,v) = (0,0),\ T = T_h,\ C = C_h \tag{22}$$

$$For\ x \in [0,L]\ ,\ y = L:\ (u,v) = (0,0),\ T = T_C,\ C = C_h \tag{23}$$

$$For\ x = [1 - \cos(2\pi k y)]/a\ \&\ y \in [0,L], k = 2:\ (u,v) = (0,0),\ \partial T/\partial y = 0,\ C = C_h \tag{24}$$

$$For\ \forall x = [a - \{1 - \cos(2\pi k y)\}]/a\ \&\ y \in [0,L], k = 2 : (u,v) = (0,0), \partial T/\partial y = 0, C = C_h \tag{25}$$

To understand the density level of nanofluid in the entire geometry, non-zero and maximum density boundary conditions must be applied to all walls, and we adopted $C = C_h$ at the rigid boundary to limit the appearance of singularities in solutions. We dimensionless the governing equations because non-dimensionalization provides the sovereignty of the inquiry, regardless of the context of some contents. The regulatory flow parameters of the system can undoubtedly be detected. By making clear statements about the importance and outline of geometry, we can gain insight into the physical issues that need to be studied. These goals can be accomplished over the fitting choice of gages. In this study, as a measure of distance, the cavity dimension of the domain under consideration is measured along the *x*-axis. The following dimensionless variable ([40]) are used to dimensionless the governing equations. (3), (4), (5), (6), (7), (8) and (9) with boundary conditions (21), (22), (23), (24) and (25):

Table 1
Water and CuO nanoparticle's thermo-physical characteristics at ambient temperature.

Items:	(c_p) $(J/(kgK))$	ρ (kg/m^3)	κ (Wm^{-1}/K)	μ $(Kg\,m^{-1}s^{-1})$	β $(1/K)$
Water (base fluid)	4.179E3	9971E-1	613E-3	1.003E-3	21E-5
CuO(material)	5318E-1	6.32E3	765E-1	–	1.8E-5

Table 2
Nusselt number $(\overline{Nu})$ comparison with those of the study in Refs. [44–46] for different values Ra_T and φ with $Ra_C = 0$ $Ha = 40$, $Le^{-1} = 0$, $\gamma = 0$ and $N_{TBT} = 0$.

	$\varphi = 0.0$				$\varphi = 0.02$	
Ra_T	Present Study	Davis [45]	Ghasemi et al. [44]	Wan et al. [46]	Current Study	Ghasemi et al. [44]
10^3	1.50463	1.118	1.002	1.117	2.34734	1.060
10^4	1.50677	2.238	1.183	2.254	2.34818	1.212
10^5	3.30602	4.509	3.150	4.598	3.26612	3.183

$$\overline{U} = \frac{\overline{u}L}{\alpha_{bf}},\ \overline{X} = \frac{\overline{x}}{L},\ P = \frac{\overline{p}L^2}{\rho_{bf}\alpha_{bf}^2},\ \theta = \frac{T - T_C}{\Delta T},\ \tau = \frac{\alpha_{bf}t}{L^2},\ \Phi = \frac{C - C_C}{\Delta C} \tag{26}$$

The dimensionless flow equations can be expressed in the form:

$$\text{Continuity equation: div } \overline{U} = 0 \tag{27}$$

$$Momentum\ equation:\ \frac{\partial \overline{U}}{\partial \tau} = -\overline{U}\cdot\nabla\overline{U} - \frac{\rho_{bf}}{\rho_{nf}}\nabla \mathrm{P} + \frac{\mathrm{Pr}\mu_{nf}}{\nu_{bf}\rho_{nf}}\nabla^2\overline{U} + F^* + \frac{\sigma_{nf}}{\sigma_{bf}}\frac{\rho_{bf}}{\rho_{nf}}\mathrm{Pr}Ha^2(\overline{U}\times\overline{B})\times\overline{B} \tag{28}$$

$$Energy\ equation:\ \frac{\partial\theta}{\partial\tau} = -\overline{U}\cdot\nabla\theta + \frac{\alpha_{nf}}{\alpha_{bf}}\nabla^2\theta + \frac{1}{Le}\frac{\nabla\Phi\cdot\nabla\theta}{\Phi + \Phi_C} + \frac{\mathrm{Pr}N_{TB}}{Sc}\frac{\nabla\theta\cdot\nabla\theta}{\theta + \theta_C} \tag{29}$$

$$Concentration\ equation:\ \frac{\partial\Phi}{\partial\tau} = -\overline{U}\cdot\nabla\Phi + \frac{\mathrm{Pr}}{Sc}\nabla^2\Phi + \frac{\mathrm{Pr}N_{TB}}{Sc}\left(\frac{\nabla\Phi\cdot\nabla\theta}{\theta + \theta_C} + \frac{\Phi + \Phi_C}{\theta + \theta_C}\nabla^2\theta\right) \tag{30}$$

$$(\overline{U}\times\overline{B})\times\overline{B} = \begin{cases} (V\cos(\chi) - U\sin(\chi))\sin(\chi), & \text{along } X-\text{momentum} \\ (U\sin(\chi) - V\cos(\chi))\cos(\chi), & \text{along } Y-\text{momentum} \end{cases} \tag{31}$$

$$F^* = \begin{cases} 0 & ,\ \text{along } X-\text{axis} \\ \frac{(\rho\beta)_{nf}}{\beta_{bf}\rho_{nf}}Ra_T\mathrm{Pr}\theta + Ra_C\mathrm{Pr}\Phi, & \text{along } Y-\text{axis} \end{cases} \tag{32}$$

The dimensionless parameters introduced in the above Eqs. (27)–(32) are as follows:

$$The\ Schmidt\ number\ ,\ Sc = \mu_{bf}/(\rho_{bf}D_B) \tag{33}$$

$$The\ local\ solute\ Rayleigh\ number,\ Ra_C = \frac{(\rho\beta^*)_{nf}}{\alpha_{bf}\nu_{bf}\rho_{nf}}gL^3\Delta C \tag{34}$$

$$The\ \mathrm{Pr}andtl\ number\ ,\ \mathrm{Pr} = \nu_{bf}/\alpha_{bf} \tag{35}$$

$$The\ Hartman\ number,\ Ha^2 = \frac{\sigma_{bf}}{\mu_{bf}}B_0{}^2L^2 \tag{36}$$

$$The\ \mathrm{modified}\ Lewis\ number,\ Le = \alpha_{bf}/D_B \tag{37}$$

$$The\ vibrant\ thermal - diffusive\ parameter,\ N_{TB} = D_T/D_B \tag{38}$$

$$The\ local\ thermal\ Rayleigh\ number\ ,\ Ra_T = \frac{\beta_{bf}}{\alpha_{bf}\nu_{bf}}gL^3\Delta T \tag{39}$$

In the control equation, a constant temperature is introduced as the ratio of the reference temperature of the solution in nanofluid to the reference temperature difference:

$$\theta_C = \frac{T_C}{\Delta T} \tag{40}$$

Also, a constant concentration is familiarized as the ratio of the

reference concentration to the reference temperature difference in the solution:

$$\theta_C = \frac{C_C}{\Delta C} \tag{41}$$

The influence of the parameters mentioned in Eqs. (33)-(41) is the focus of this article. In the dimensionless form, the primary and peripheral conditions for the current problem are:

At $\xi = 0$, throughout the system dominion:

$$(U, V) = (0,0),\ \theta = 0,\ \ \Phi = 0,\ \mathrm{P} = 0 \tag{42}$$

For $\xi > 0$, along the bottom heated surface:

$$(U, V) = (0,0),\ \theta = 1 \quad \forall\, Y = 0,\ X \in [0,\ 1] \tag{43}$$

Along the left side wall:

$$(U,\ V) = (0,0),\ \theta = 0,\ \forall\, X = [1 - \cos(4\pi Y)]\,/\,a,\ Y \in [0, 1] \tag{44}$$

Along the right-side wall:

$$(U,\ V) = (0,0),\ \theta = 0, \quad \forall\, X = [a - \{1 - \cos(4\pi y)\}]\,/\,a,\ Y \in [0, 1] \tag{45}$$

Along the upper colder wall:

$$(U,\ V) = (0,0),\ \theta = 1, \quad \forall \quad X \in [0, 1],\ Y = 1 \tag{46}$$

The average velocity magnitude of the flow is given by,

$$V_m = \sqrt{U^2 + V^2} \tag{47}$$

The components of the fluid velocity U and V are represented by the stream function ψ as follows:

$$U = \frac{\partial \psi}{\partial Y}, \quad V = -\frac{\partial \psi}{\partial X} \tag{48}$$

The heat flux percentages on the enclosure's perimeter wall can be calculated using the local Nusselt number (non-dimensional number).

$$Nu_L = -\frac{\kappa_{nf}}{\kappa_{bf}} \frac{\partial \theta}{\partial Y} \tag{49}$$

The average heat transfer in terms of mean Nusselt number at the lower heated surface is written as

$$\overline{Nu} = -\frac{\kappa_{nf}}{\kappa_{bf}} \int_0^1 \frac{\partial \theta}{\partial Y}\, dX \tag{50}$$

3. Methodology

The finite element scheme is one of the best ways to find the solution of the fluid dynamics coupled nonlinear partial differential equations. Galerkin's extension of finite element method over the present partial differential equations is well described by Refs. [41,42]. In these procedures, the nonlinear coupled equations are translated to the weighted residual equations. The finite element procedures on the present governing equations have been analyzed by Uddin and Rahman [43]. The whole area of the system is partitioned into the fixed and non-uniform deltoid elements (called meshes). Relating temperature, concentration, and velocities by using six-node deltoid grids and pressure by using corner nodes only, the finite element equations are evaluated. For the continuity constraint, the rate of changes of pressure are chosen identical between the x and y-momentum equations as well as a lower order multinomial. Considering unvarying pressure with a linear element while discontinuity among elements, the governing equations are converted to a scheme of integral equalities by applying Galerkin weighted residual technique. Each term of the integral equalities is then solved by the exact integration formula. The suggested wall conditions are implemented to regulate the nonlinear scheme of the arithmetic equalities. The set of simple nonlinear mathematical equations is solved in a matrix format. The global matrix solutions are achieved using the Newton-Raphson repeating technique and Euler backtrack procedures. The results of this study were acquired using a partial differential equation solver with a MATLAB interface. The arithmetic results' convergence threshold, as well as error estimation, has been set at $\left|\mathrm{M}^{m+1} - \mathrm{M}^{m}\right| \leq 10^{-5}$, where M is the universal dependent variable (U, V, θ, Φ) and m is the number of iterations.

Formation of Grids is a method of defining a realm as a collection of finite element subdomains. One of the stages essential before obtaining the problem's result is the grid's uniqueness. The variables are calculated in various locations that are determined by the number grid. The quality measures of refined mesh for the expected domain under investigation are very important for numerical simulations. A quality of 1 is the best possible that indicates an optimal element in the chosen quality measure. On the other hand, a quality measure below 0.01 is low quality mesh and should be avoided in most cases. As per the authors' knowledge, the meshing algorithms in the simulation tool, COMSOL Multiphysics always attempt to escape the low-quality elements. In our problem, the quality of the mesh is measured in an extremely judicious manner with a series of examinations. For our simulation, we have considered mesh with the following quality measures: maximum growth rate is 4.176 where the average growth rate in the entire geometry is 1.286, the minimum quality measure is 0.1136 where the average quality measure is 0.896, and element area ratio is 0.01837 where the mesh area is 0.9 square meter.

This is essentially a distinct illustration of the physical field on which the problem should be resolved. An important analysis of the simulation is the freedom on the number of geometry grids. In the present work with CuO–H_2O nanofluid, an extensive mesh test method is followed to assure a grid-free result. The static values used in the simulation are $n = 3, Ra_c = 1 \times 10^4, \varphi = 0.025, Ra_T = 2.3 \times 10^5, d_p = 10nm,$ at $\tau = 2$. The study bear in mind the sphere-shaped nanosolids. We scrutinized meshes comprising 234, 362, 604, 1490, 2344, 6382, 16,852, and 24,766 components. The measures of $\overline{Nu}$ at the heated field is depicted in Fig. 2 for the grids.

Code validation is an essential practice of numerical dynamics after grid independence studies. By comparing data in stable cases, the current numerical code is validated by Refs. [44–46]. In the presence of magnetic fields [44], studied the 2D natural conduction flow in a quadrangular cavity occupied with Water-Alumina nanofluids. Considering no nanofluid concentration equation and the inclination angle ($\gamma = 0^0$) of the hydromagnetic field parameter ($Ha = 40$) are discussed with the kinetic equations for a similar study with those of [44]. The current numerical code achieves a remarkable agreement with those of [45]. We also compared the current numerical code's result to standard numerical results from Refs. [45,46], which consider an air-filled square cavity where Pr = 0.7.

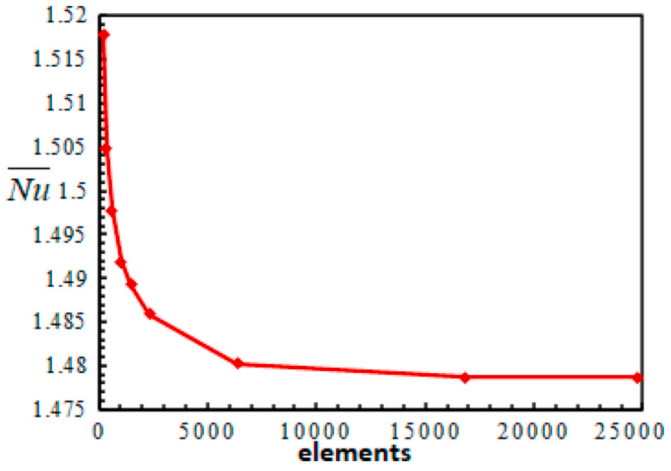

Fig. 2. Mean Nusselt number for various grid resolutions.

4. Results and discussion

The outcomes are presented as streamlines, velocity magnitude contour, isotherms, and isoconcentrations. Various line graphs were shown to understand the heat transfer rate at the corresponding time. The physical properties of nanofluids are calculated via the physical properties of nanosolids and bulk fluid displayed in Table 1. The parameters entered into the problem are varied as $Ra_T = 10^4 - 10^6$, $Ha = 0 - 60$, $\varphi = 0.025 - 0.1$, $\chi = 0^\circ - 90^\circ$, $k = 0 - 5$ and $dp = 1 - 50\ nm$. The other parameters of the problem are dependent on the physical relations and thermophysical values of nanofluids. The results of the current problem have been discussed from the physical and engineering points of views. The defined ranged of the parameters of the problems are produced convergent results throughout the cases and any instability occurrence were absent within the marked ranges of the parameter values. The detailed instability analysis of the parameters of the present analysis can be obtained in the study of Uddin and Rahman [3].

Fig. 3 illustrates the consequences of nanoparticle volumetric fraction φ and thermal Rayleigh number Ra_T on the streamlines. Significant changes in the streamline patterns occur due to the changes of the Rayleigh number with the variation of the nanoparticle volume fraction. Overall, the higher value of the Rayleigh number($Ra_T = 10^6$) and the lower concentration of nanofluid ($\varphi = 0.025$) enhances the fluid velocity. For all the cases, multiple sets of symmetric small and big vortices arise inside the cavity which is a clear indication of the normal nature of the convection heat transfer. In most of the cases, strong velocity layers are formed among the oppositely rotating vortices. Additionally, two velocity boundary layers also appear along the wavy side walls. As can be observed that, for the lower thermal Rayleigh number ($Ra_T = 10^4$) and all values of the nanoparticle volume fraction ($\varphi = 0.025,\ 0.05,\ 0.1$) the streamlines are thin, weak, and extended along the horizontal walls. This clearly indicates the production of convective heat transfer inside the cavity. Also, the cores of the whirlpools are formed near the curvy sides of the enclosure for the presence of the vigorous temperature gradient in those regions. A certain rise in the Rayleigh number ($Ra_T = 10^5$) brings significant change in the streamline's arrangement. For the lower amount of nanofluid mass, a large anticlockwise rotating vortex arises centering at the middle and occupying the maximum area of the cavity. But for the augmentation of particle volumetric mass ($\varphi = 0.05,\ 0.1$), four pairs of similar, symmetric, and oppositely rotating smaller vortices form along the wavy peaks of the side walls. For, ($Ra_T = 10^5$) and($\varphi = 0.025$) the core of the maelstrom formed at the locus of the inclusion but for ($Ra_T = 10^5$) and ($\varphi = 0.05,\ 0.1$) they appear on each vortex near the wavy peaks due to the occurrence of the forceful temperature gradient in those parts. The fluid velocities in the above mentions cases seems insignificant due to the lack of particles in fluid motion. The velocity boundary layers are also feeble and are formed among the vortices and near the wavy walls for the formation of temperature gradient. As the Rayleigh number increased by five to ten times i.e., ($Ra_T = 5 \times 10^5,\ 10^6$), extensive rise in the fluid velocity can be found due to the attenuation of nano solids mass. Strong thermal gradients formulated inside the whole domain of nanofluid including the boundaries of the cavity. The compactness of the streamlines declines and becomes prominently robust and extend vertically showing the augmentation of maximum fluid velocities. For $Ra_T = 5 \times 10^5,\ 10^6$, the streamlines are uniform for higher concentration of nanoparticles ($\varphi = 0.1$) but distorted for $\varphi = 0.025,\ 0.05$. The depth of the velocity border layers on the cooler wall intensifies. The centers of the convection vortices have a leaning towards forming at the middle of the vessel. Also, tiny cells are formed in the enclosure's upper and lower corners. The breadth of the consequential velocity layer among the whirlpools reduces. This clearly indicates greater rate of heat transport owing to the creation of strongly rotating convection cells inside the whole enclosure for higher Rayleigh number. These are the aftermath of the enhanced temperature variances within nanofluid which produce advanced buoyancy power in the crater. At the corners of the cavity, the fluid velocity is higher near the wavy troughs due to the temperature gradient created by the higher Rayleigh number.

For the lower value of Rayleigh number ($Ra_T = 10^4$) and all values of the nanoparticle volume fraction ($\varphi = 0.025,\ 0.05,\ 0.1$), two bigger clockwise and anti-clockwise rotating vortices emerge inside the enclosure with two smaller vortices at the upper corners of the cavity. The streamlines are feeble little bit twisted but arranged along the wavy walls of the geometry. As the Rayleigh number enhances by ten times

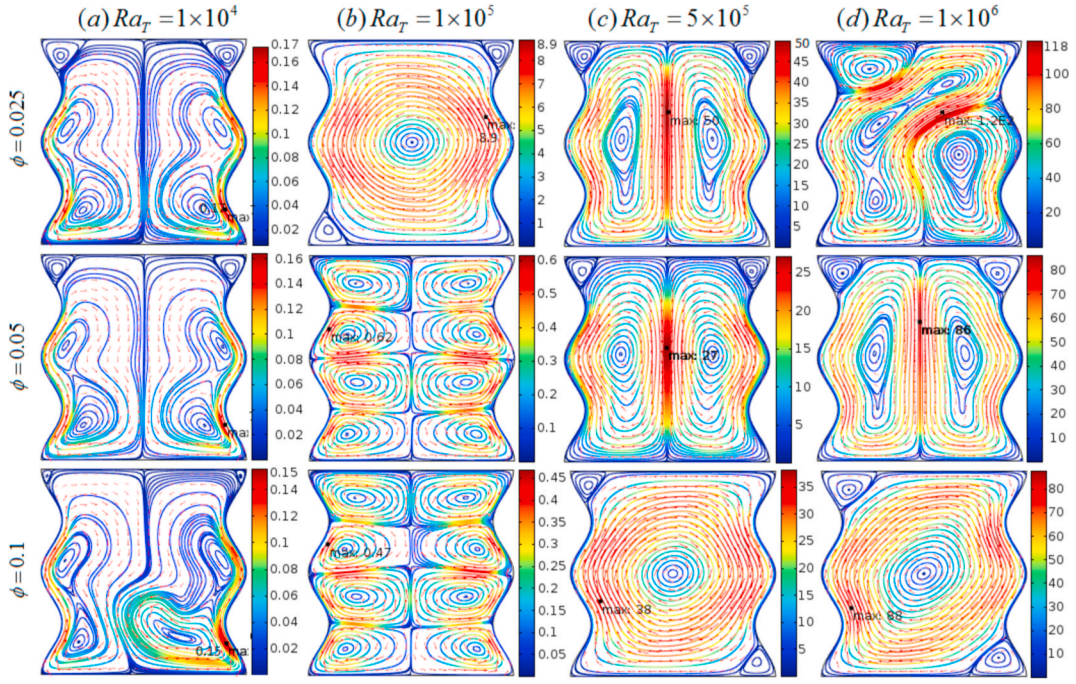

Fig. 3. Streamlines for the nanoparticle volume fraction φ and thermal Rayleigh number Ra_T for the fixed nanoparticle diameter, $dp = 10$ nm, $Ha = 40$, $\chi = 0$ at $\tau = 2$.

(1×10^5) and for $(\varphi = 0.025)$ a bigger anti-clockwise revolving vortex appears inside the enclosure with two smaller at the lower left and upper right corner of the vessel. However, increasing the volumetric portion of nanofluid results in the formation of eight identical vortices in two pairs that revolve in opposite directions.

Fig. 4 represents the velocity magnitude contour for various values of φ and Ra_T. As the volume fraction of nanoparticles increases, the change in velocity is not large for lower buoyancy $(Ra_T \leq 10^4)$, but for higher buoyancy, the velocity changes significantly. The higher velocity amplitude appears at the lower values of φ (≤ 0.025) and at the higher values of thermal Rayleigh number $(Ra_T \geq 10^6)$. For the lower values of Ra_T, as the volume fraction of nanoparticles increases, the velocity decreases gradually. In addition, the eddy currents are made adjacent to the wavy walls of the geometry. A strong velocity boundary layer is formed at each of the vertical walls indicating the insignificance of flow velocity inside the core of the cavity. The lower temperature difference in the fluid flow is the reason for the adverse effect on the velocity intensity. For a higher Rayleigh number $(Ra_T \geq 10^5)$, as the volume fraction of nanoparticles increases, multiple velocity loops are formed in the entire domain, leading to the disappearance of the velocity boundary layer, the strength and elongation of the velocity loop increases. These are the results of the leading effect of nanoparticles, in which the vertical wavy surface and bottom heating wall enhance the movement of the particles. At the nanoparticle volume fraction $\varphi = 0.025$, the enhancement in the buoyancy force from 10^4 to 10^5, the velocity intensity remarkably enhances (almost 9 times) whereas the change in the buoyancy force from 10^5 to 10^6, the velocity magnitude increases largely by almost 109 times. On the other hand, when $\varphi = 0.1$, when the buoyancy is increased from 10^4 to 10^5, the velocity magnitude is increased by 3 times, and when the buoyancy is increased from 10^5 to 10^6, the velocity magnitude is increased by nearly 87 times. Hence the more nanoparticles in the base fluid, the greater the force required in the flow to maximize the velocity intensity, indicating that the occurrences of the higher velocity amplitude largely depend on the combination of φ and Ra_T. For, the change in φ from 0.025 to 0.1, the velocity magnitude decreases by a decrease of 26.27%. For $Ra_T = 10^6$, the change of φ from 0.025 to 0.1 reduces the speed range by 26.27%, while for $Ra_T = 10^4$ and for similar changes in φ, the velocity magnitude is reduced by nearly 12%.

The isotherm contour is displayed in Fig. 5 for the three values of nanoparticle volumetric fraction and four distinctive values of Ra_T. The nanoparticle volumetric fraction and the thermal Rayleigh number control isotherms. The strength of the isotherm increases as the thermal Rayleigh number rises, and adding more and more nanosolids to the base fluid reveals the ideal buoyant force need. For the lower value of $(Ra_T \leq 10^4)$, throughout cases of nanoparticle volume fraction, conduction dominates, and feeble isotherm is observed in the middle of the vessel, and only a slight convection happens near the wavy surfaces. For the Rayleigh number $(Ra_T = 10^5)$, convection governs inside the enclosure while, for $\varphi > 0.025$, the conduction form of heat transport occurs and, in this instance, the heat lines condensed to the heated bottom wall because of the higher viscosity of nanofluid. For, $(Ra_T > 10^5)$, convection dominates inside the cavity for all the cases of nanomaterial volumetric portion. The isotherm lines are upper parabolic shape for $\varphi \leq 0.05$ while isotherm lines are downward curve for $\varphi > 0.05$. Note: More convoluted isotherm lines occur for $Ra_T = 10^6$ and similar pattern of isotherms observes for the higher nanoparticle volume fraction in this case. This indicates that nanofluid having lower nanoparticle volume fraction produces early convections whereas for the higher volume fraction, nanofluids absorbs heat and it engrosses more forces to reach its optimal capacity.

Fig. 6 shows the state of the isoconcentrations for three values of φ and four values ofRa_T. The labeling of the isoconcentration indicates whether the particle distribution in the fluid is uniform or not. The labeling of $O(1)$ represents the highest labeling in which the particle uniformity in the solution occurs. As can be seen from the figure that the isoconcentration pattern is almost same as the streamline pattern. This might be happened due the fact that the nanofluid flow pattern reflects dominantly in the loop of isoconcentration. When the Rayleigh number is low, a uniform isoconcentration with the largest labeling appears in the upper part of the cavity, and a poor isoconcentration distribution appears in other parts of the container due to the low temperature difference in the fluid. The enhancement of the thermal Rayleigh number

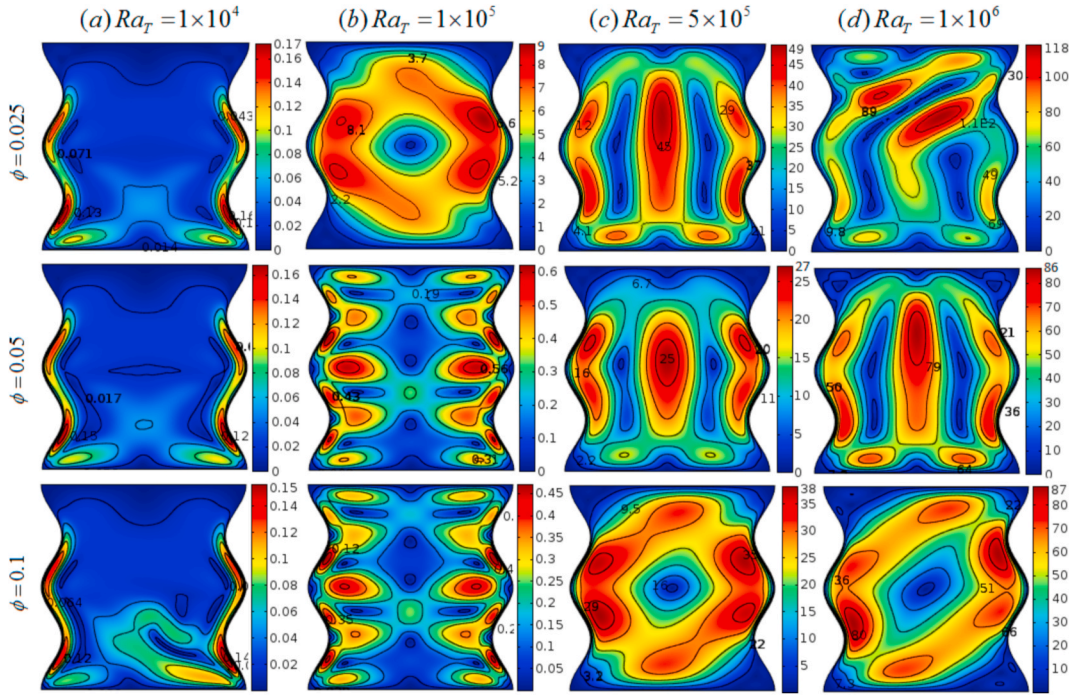

Fig. 4. Velocity Magnitude for the nanomaterial volumetric segment φ and thermal Rayleigh number Ra_T for the installed nanoparticle length, $dp = 10$ nm, $Ha = 40$, $\chi = 0^o$ at $\tau = 2$.

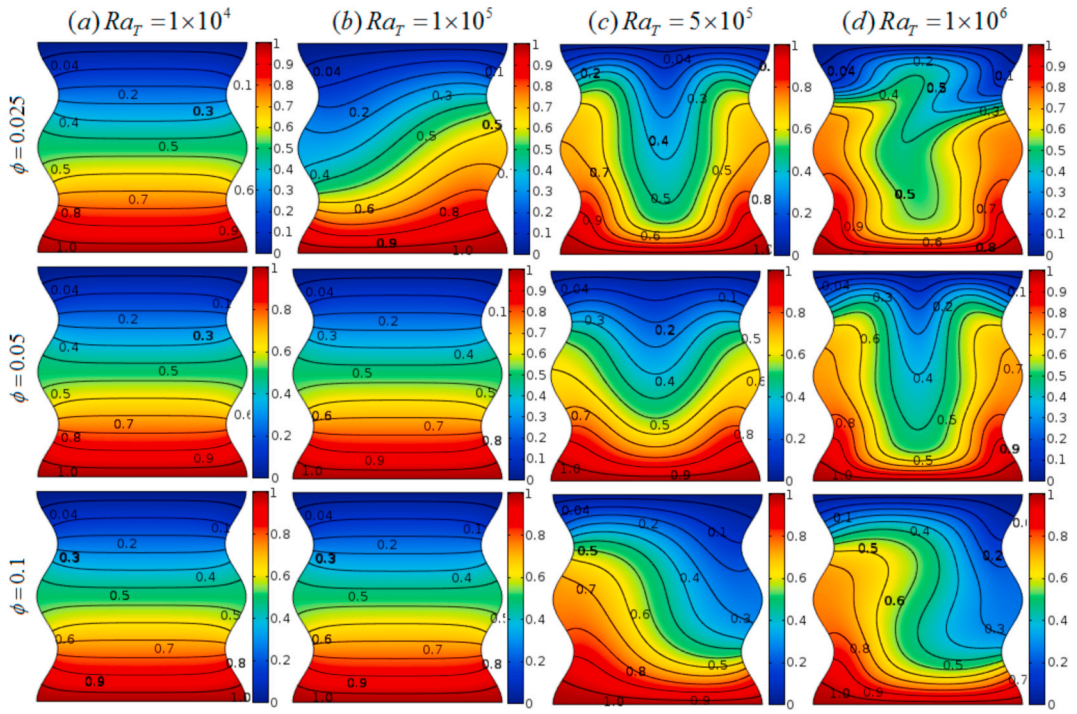

Fig. 5. Isotherms for the particle volume fraction φ and thermal Rayleigh number Ra_T for the fixed nanoparticle length, $dp = 10$ nm, $Ha = 40$, $\chi = 0^o$ at $\tau = 2$.

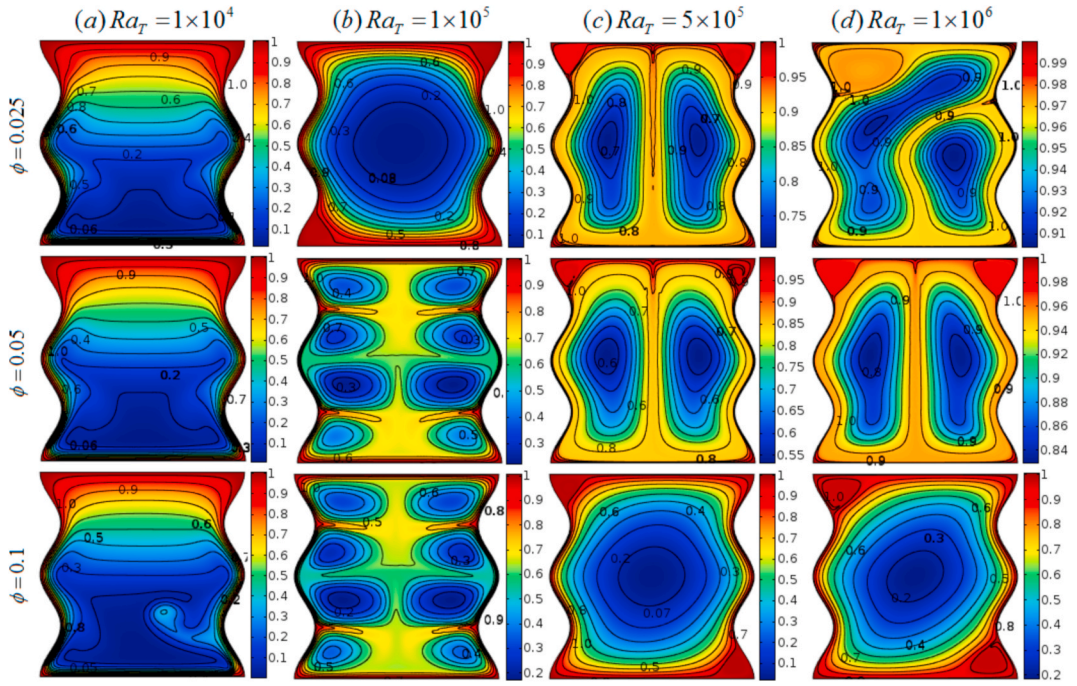

Fig. 6. Isoconcentrations for the nanomaterial volumetric portion φ and thermal Rayleigh number Ra_T for the particular nanomaterial diameter, $dp = 10$ nm, $Ha = 40$, at $\tau = 2$.

enhances the loops and the labeling of the isoconcentration in the entire cavity. Due to the lack of particle motion within the vortex, poor labeling in the circulatory core were witnessed in all cases. For a higher Rayleigh number, labeling of the isoconcentration loops almost reaches the peak, indicating the best distribution of molecular species in the fluid. Also, two strong small eddies can be seen at the position where the labeling extents the maximum. For the increase of the nanoparticle volumetric portion, the intensity of the isoconcentration decreases slightly in all cases, which is due to the accumulation of more nanoparticles into the fluid molecules, resulting in higher viscosity. In addition, the ring strength of isoconcentration depends on the number of nanoparticles within the normal fluid and the adjustment of the buoyancy force. Note: Strong buoyancy is required to stimulate the fluid substance in the higher nanoparticle volume fraction, which can produce a uniform isometric distribution with the desired label.

Fig. 7 demonstrates the time verses mean Nusselt number for the

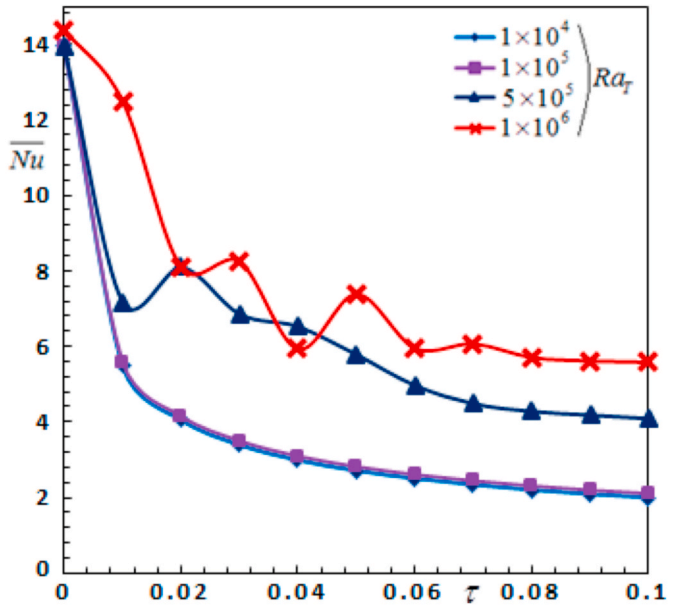

Fig. 7. Mean Nusselt number with respect to time and several thermal Rayleigh numbers for $\varphi = 0.025$, $dp = 10$ nm$Ha = 40$, $\chi = 0^o$.

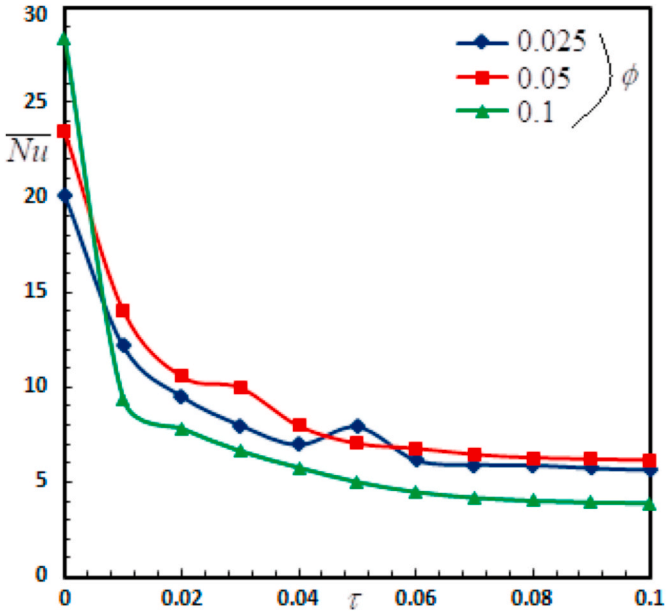

Fig. 8. Mean Nusselt number with respect to time and several nanoparticle volume fraction for $Ra_T = 1 \times 10^6$, $dp = 10$ nm, $Ha = 40$, $\chi = 0^o$.

different Rayleigh numbers. Initially, the average Nusselt number was maximum which declines gradually as the time passes for all values of the thermal Rayleigh numbers until for a certain time and then it becomes plateau. As the Rayleigh number increases from 5×10^5 to10^6, the average Nusselt number rises significantly while, the intensification in the Rayleigh number from 10^4 to10^5, the similar mean Nusselt number has been obtained. A striking change in the mean Nusselt number happens for $Ra_T \geq 10^5$ and at$\tau = 0.05$, for the increase in $Ra_T = 10^5$ to5×10^5, the mean Nusselt number enhances by 105.4%. Therefore, $Ra_T = 10^5$ is the critical Rayleigh number for the present investigation. For the higher Rayleigh number ($Ra_T \geq 10^5$), average Nusselt number fluctuates and overlaps to each other until a fixed time and after that it remains the same. We observe that specifically for $Ra_T = 10^5$ 5×10^5, and 10^6, the mean Nusselt number becomes steady state at $\tau = 0.09$ 0.08, and 0.075 respectively. Hence, the higher Rayleigh numbers results the early steady state solution. The average heat transfer of the heat Rayleigh number from 10^3 to 10^4 remains stable. Whenever it increases to 10^6, the mean heat transport surges by 158.70%.

Fig. 8 expresses the mean Nusselt number on the lower heated wall with respect to time for the variations of nanoparticle volume fraction. As time elapses, the average heat transfer rate decreases gradually until it reaches a steady state. At the beginning of the process ($\tau = 0$), the mean Nusselt number of all values of nanoparticle volume fraction at the bottom wall is the largest, and in a short period of time ($\tau = 0.01$) drops suddenly, and then gradually decreases until it stabilizes at $\tau = 0.1$. However, for all nanoparticle concentration levels, the average Nusselt number fluctuates from $\tau = 0.01$ to $\tau = 0.06$. Initially, the maximum and minimum average heat transfer rates appear in the nanoparticle volume fractions $\varphi = 0.1$ and $\varphi = 0.025$, respectively. However, in steady state, the lowest and highest average Nusselt numbers appear on $\varphi = 0.1$ and $\varphi = 0.05$, respectively. In addition, when $\tau = 0.05$, compared with $\varphi = 0.1$, the mean thermal transmission rate for $\varphi = 0.05$ and $\varphi = 0.025$, are increased by nearly 40% and 80%, respectively, while the opposite is true when $\tau = 0.1$. Finally, the average Nusselt number for $\varphi = 0.025$, reaches the deterministic stage earlier than the other concentration levels. The average heat transfer increases by 10.18% for the change in the nanoparticle volume fraction from, 0.025 to 0.05.

The significant effects of hydromagnetic field on the flow-lines, velocity magnitude, isotherms, and isoconcentrations are displayed in Fig. 9. Without the presence of the magnetic field, a strong rotational flow has been observed. Due to the higher flow intensity, two small vortices are visible in the topper and lower corners of the vessel, two resilient velocity loops are circulated in the entire disk, convective mode of heat transfer and almost uniform labeling of concentration contour showed inside the whole cavity. For the presence of the hydro-magnetic intensity, the state of the convective flow pattern and the concentration of nanofluid declines remarkably. Also, when the Hartmann number increases, many changes are observed such as streamlines loosely connected and elongation towards the corners decreases and rotational bog vortex is visible in the middle, small vortices become very weak, the flow intensity declines, the loops of the velocity amplitude lose the strength, the state of the convective mode changes to the conduction mode and the uniformity of the concentration labeling significantly deteriorated. These all happens because the magnetic dipole has uniformly distributed even in the case of the higher intensified magnetic field and the velocity magnitude, and the temperature have significantly declined with the intensified magnetic field due to the dominating viscous force. The viscous force increases with the increases in magnetic force in this case. The magnetic dipole always tends to guide the flow of nanofluid in its own direction.

For the variation of the Hartmann number, Fig. 10 depicts the mean Nusselt number at the boundary walls with respect to time. In the passage of time, the average heat transfer rate significantly decreases up to obtaining a definite value. The nonappearance of the magnetic intensity ($Ha = 0$) produces higher rate of average heat transfer while lower and similar appears for $Ha \geq 40$. This happens due to the scattered state of the nanoparticles in the fluid which requires time to be distributed uniformly. At $\tau = 0.01$, the mean Nusselt number falls suddenly near a certain value for all $Ha \geq 20$ while it remains almost steady for $Ha = 0$ then subsides smoothly until reaching to a plateau except for the case $0 < Ha < 40$. However, the heat transport rate attains a definitive value earlier for $Ha = 20$ in comparison to other values of Ha. This indicates that, in this current arrangement higher magnetic intensity should not be applied. Because it would increase the timing to reach the average heat transport rate to a steady state. Since, the mean Nusselt number lines coincide for $Ha \geq 40$, hence, we can say that $Ha = 40$, is our critical Hartmann number for the present study. We have calculated that the average heat transfer declines by 64.08% if the value of the Hartmann number changes from 0 to 40.

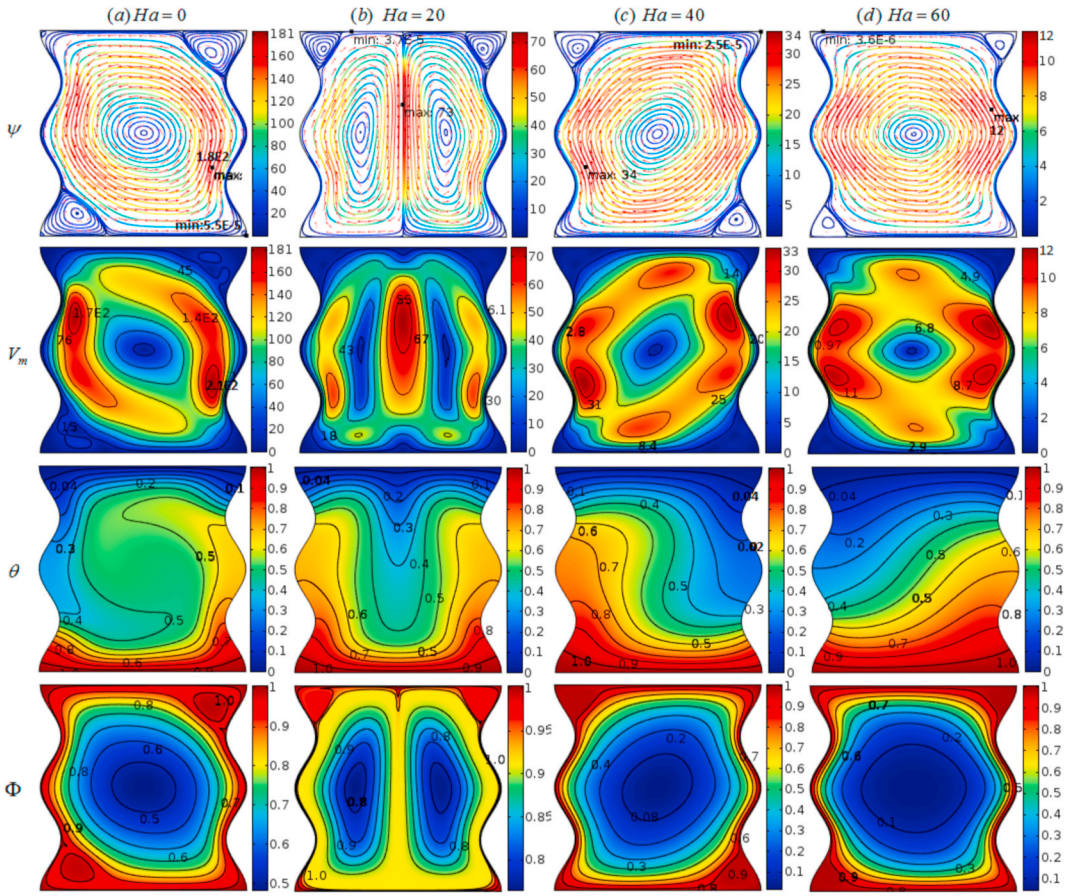

Fig. 9. Effect of the Hartman Number (Ha) for $dp = 10$ nm, $\varphi = 0.025$, $Ha = 40$, $Ra_T = 2.3 \times 10^5$ at $\tau = 2$.

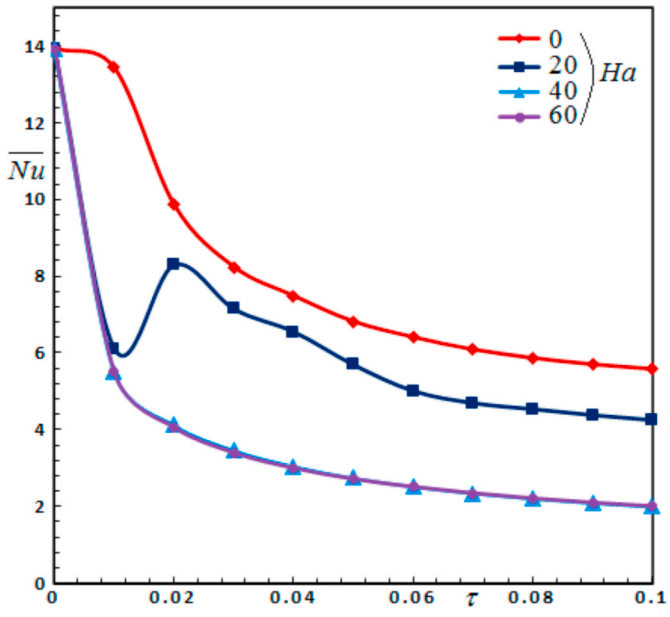

Fig. 10. Average heat transfer rate (Nusselt number) with respect to time for various Hartmann numbers when $Ra_T = 2.3 \times 10^5$, $\varphi = 0.025$, $dp = 10$ nm, $Ha = 40$, $\chi = 0^o$.

Fig. 11 shows the effects of the magnetic field inclination angle. We have seen that the flow patterns significantly get in the way by the magnetic field tilted angles. As the magnetic field leaning angle surges from 0° to 90°, the stream, thermal, and absorption fields are intensified. An increase of 202.94% in velocity magnitude has been observed for the rise in the magnetic field inclined turn from 0° to 90°. The similar flow, thermal, and the concentration patterns are observing for the various magnetic inclination angles, $30^\circ \leq \chi \leq 60^\circ$. In this case, a large vortex rotates counterclockwise, and the velocity amplitude field contains two strong vortices elongated left and right, and the hot wires are distributed in the cavity in the shape of cube roots. The isoconcentration loops are like that of the streamlines. Contrarily, absolute differentiated patterns flow and thermal filed are ranked in the cavity for the magnetic inclination angle of $\chi = 0^\circ$ and $\chi = 90^\circ$. For the case, $\chi = 0^\circ$, a large vortex rotates clockwise, and two small vortices are visible at the corners of the cavity. The velocity magnitude loops are strong in the middle of the cavity and the two loops in the middle vertically distributes. The thermal lines are distributes following the shape of the negative cube roots. The effects of the magnetic inclination $\chi = 90^\circ$ are significantly positive and different than the other cases. The flow fields are divided into two big vortices. Two large symmetrical vortices are oppositely rotated in the cavity shows strong a flow field. The velocity magnitude contours are divided in five loops and are spreads in the entire cavity. The thermal fields are upward parabolic shape shows higher convection manner of heat transport. The uniform labeling of isoconcentration looks like the streamline in this case. In this case, since the route of the magnetic force is consistent with the route of the fluid flow, the fluid flow direction and the magnetic force act on gravity together, so a strong thermal field and a flow field are observed.

Fig. 12 shows the relationship between the dimensionless time and the average heat transport rate at the lower boundary with respect to the change in the leaning of the magnetic intensity. It can be observed from the line graph that the mean Nusselt number has changed significantly as the leaning of the applied magnetic field strength increases with time. Initially, although the average Nusselt number of all inclination angles

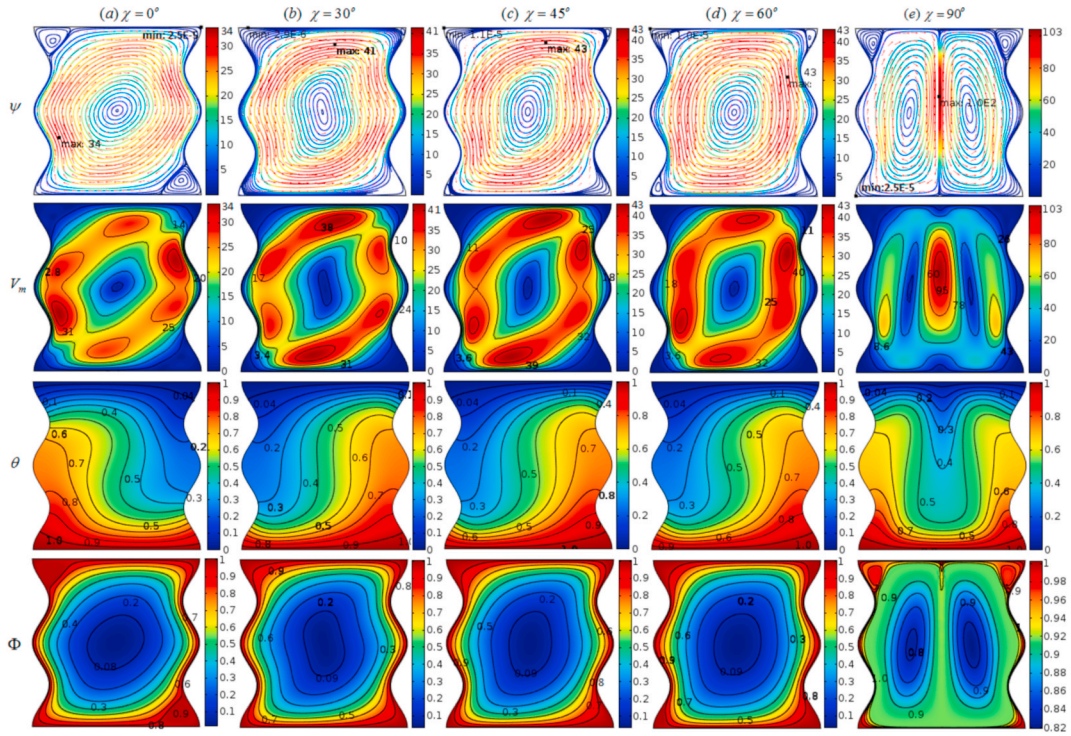

Fig. 11. Magnetic field inclination effect for $dp = 10$ nm, $\varphi = 0.025$, $Ha = 40$, $Ra_T = 2.3 \times 10^5$, at $\tau = 2$.

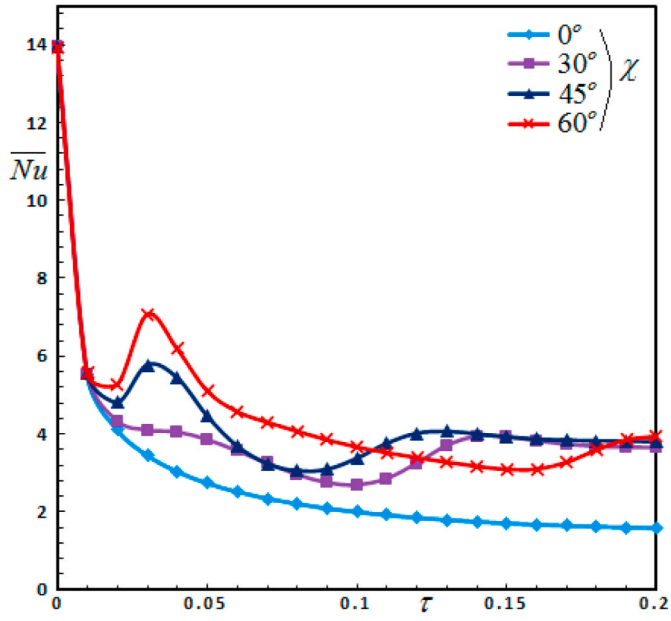

Fig. 12. Mean Nusselt number with respect to time and inclination angle (magnetic field) when $Ra_T = 2.3 \times 10^5$ $\varphi = 0.025$, $dp = 10$ nm, $Ha = 40$.

has the same value, it suddenly drops in a short time ($\tau = 0.01$) due to the continuous heat transfer process. However, the mean value of the Nusselt expression oscillates at all tilt angles except the horizontal tilt angle until a stable value is obtained. When a magnetic field is applied along the heated wall, the average heat transfer rate gradually decreases until it becomes stable. For the inclination angles $\chi = 30^o, 45^o$ and 60^o; the mean Nusselt number rises sufficiently at $\tau = 0.03$ but falls and upsurges until it reaches to a steady-state. It should be noted that each escalation in the slant of the magnetic pitch strength requires more time to obtain a definite amount of the mean Nusselt sum. The steady value of the mean Nusselt number occurs at $\tau = 0.19$ for all inclination angles. If the magnetic pitch gradient slope shifts from 0° to 60°, the average heat transfer increases by 148.85%. However, the stable maximum average heat transport arises whenever the leaning angle of the magnetic field is 60^o.

The effects of the number of waves on the vertical surfaces are demonstrated in Fig. 13. We have observed that the wave number significantly impacts on the pattern of the various field's distribution in the enclosure. The flow and thermal intensity can be managed by the wave number. For no wave on the vertical walls, the streamlines are distributed in an upward trend, and there are two large eddies are visible near the heated wall, the core is firm, and the velocity strength is significantly higher in this case. With the introduction and increase of waves on the vertical wall, the streamlines core increases, the core elongates vertically, capturing the entire cavity along the surface wave pattern, and the speed decreases slightly, indicating that the fluid flow can be controlled by the surface structure of the flow domain. Also, trivial vortices molded on the upper corners of the cavity in this case. The velocity distribution has a similar pattern to the streamline distribution, and this effect can be observed in the entire wavenumber. As we have seen, due to the vertical wave surfaces, many small velocity magnitude loops are formed, and they increase as the wave number increases. For a vertical non-wave wall, the isotherm looks like a lamp, blooming to the upper wall, like a downward parabola, but in the case of a wavy wall, it is an upward parabola. This shows that isotherms patten can be controlled by the surface wave number. In addition, the labeling of isoconcentration increase via the rise of the wave number, showing that the uniformity of the species increases in the domain.

The effect of wave numbers of the side walls on the average heat transport rate with respect to the dimensionless time has been shown in Fig. 14. As can be seen from the line graph, the enhancement of waves on the side walls significantly increases the heat transport rate. Starting from certain higher values, the rate falls rapidly within a moment ($\tau = 0.015$) then increases a bit up to $\tau = 0.03$ for $k = 2 - 5$ and for $k = 1$, it declines gradually until obtaining a definite state. From the lines, it is also evident that the single peak exhibits much higher average heat

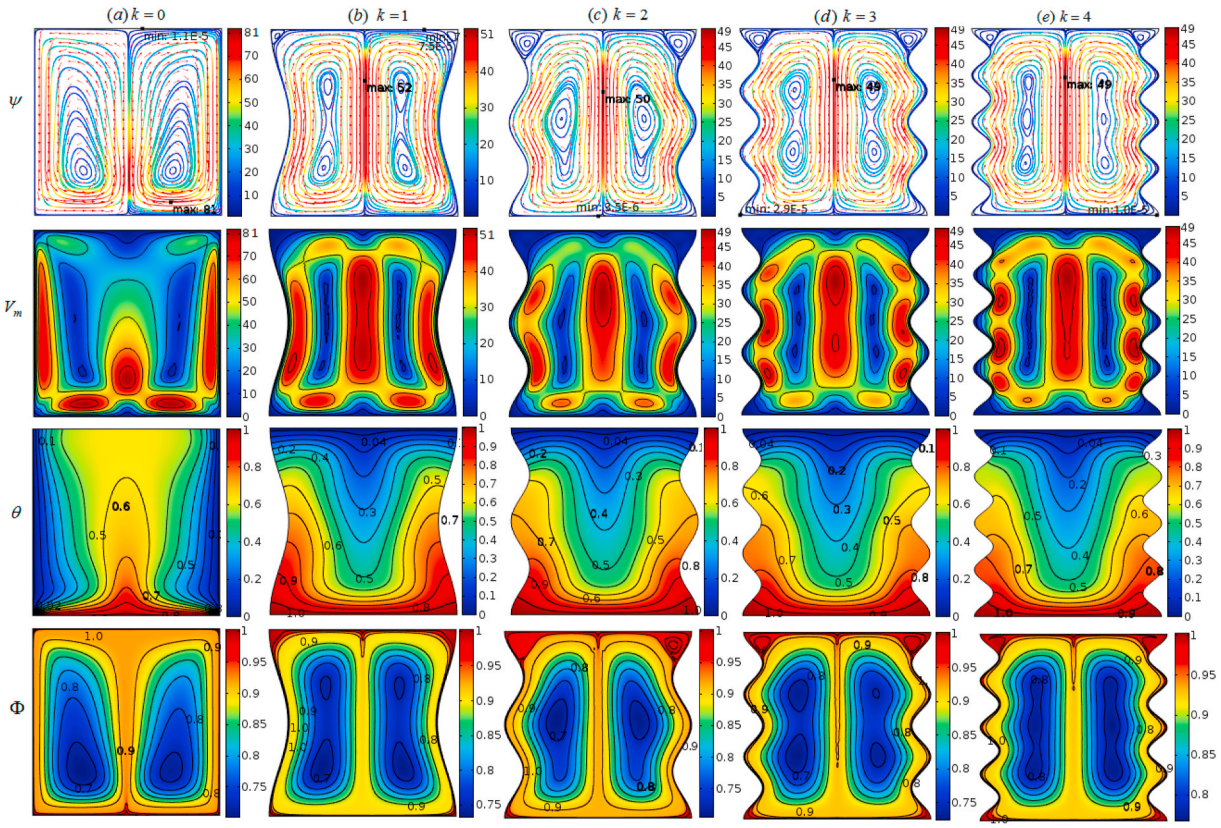

Fig. 13. Wave number effects for $dp = 10$ nm, $\varphi = 0.025$, $Ha = 40$ $Ra_T = 5 \times 10^5$, $\chi = 0^o$ at $\tau = 2$.

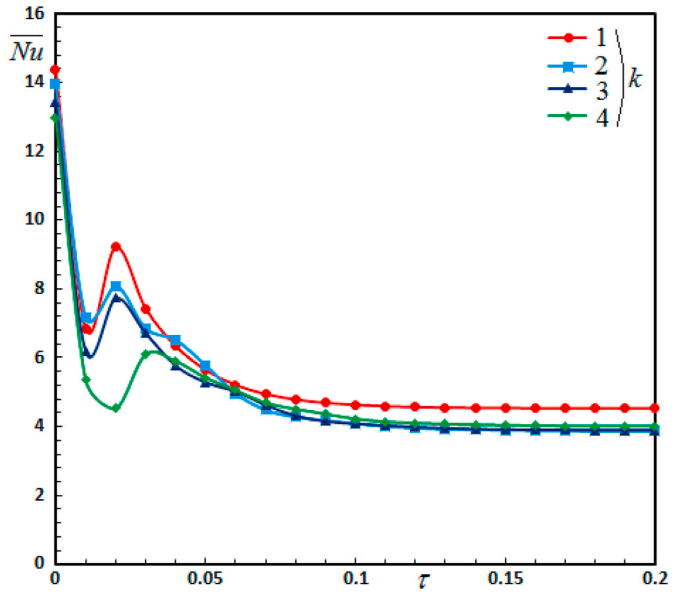

Fig. 14. Mean Nusselt number with respect to time and wave number (k) when $Ra_T = 2.3 \times 10^5$, $\varphi = 0.025$, $dp = 10$ nm, $Ha = 40$, $\chi = 0^o$.

transmission rate then for the number of peaks $k > 1$. For $k = 2 - 5$, the average heat transfer improves about 180–200% in comparison to during the time of steady-state solution. However, it is crucial to mention that the mean Nusselt number becomes stable earlier for the increment of the number of wavy peaks of the side walls. Also, the extreme heat transport rank is found from the case for $k = 1$.Importantly, we have incisively calculated that the non-wave vertical surface of the container has a higher heat transport percentage. When the wave number is increased to 2, the heat transfer is reduced by 16.98%, and when the wave measure is amplified from 2 to 4, the thermal transfer rate is increased by 3.62%.

Fig. 15 shows the effects of the particle diameter on streamlines, velocity magnitude, isotherm and isoconcentration. The particle size of 1 nm exhibits a powerful vortex rotating in the shell, and similar effects appear in isotherms, velocity amplitude contours, and isoconcentration distributions. Specifically, the particle size less than 5 nm has a comprehensive effect on the flow field and thermal field. The streamlines become elongated diagonally to the right, and there are small vortices for smaller nanoparticle sizes, which indicates that the resultant speed in the shell is higher. For nanoparticles larger than 2 nm, the streamline is clearly divided into two vortices. In this case, a velocity layer will also be formed between the vortexes in the middle of the shell. A higher convection pattern can be seen in the smaller particle size. The isotherm is obviously complicated, showing higher convection for particle diameters smaller than 5 nm, while the isotherm is an upward parabola in various nanoparticle sizes larger than 5 nm. The isoconcentration labeling of particle sizes smaller than 5 nm becomes almost uniform, while for particle sizes larger than 5, the flow field and thermal field of each particle size are almost similar. For a particle of size 30 nm, the uniform concentration state is loosely connected, and the particles tend to gather on the surface. In the middle of the cavity, it shows a very poor distribution. In this case, in order to distribute the particles uniformly, a larger external force may be required.

Nanoparticle size is important in heat transfer engineering. Due to the small size of nanoparticles, the flow behavior of nanofluids has been significantly diversified, and research on them has increased over the decades. Hence, the consequences of the nanoparticle diameter on the mean Nusselt number in regard to the dimensionless time has been depicted in Fig. 16. The line graph shows the decline of heat transport rate with the advancement of the time for the variations in dp, until a fixed value is obtained. In the absence of the fluid motion, the heat

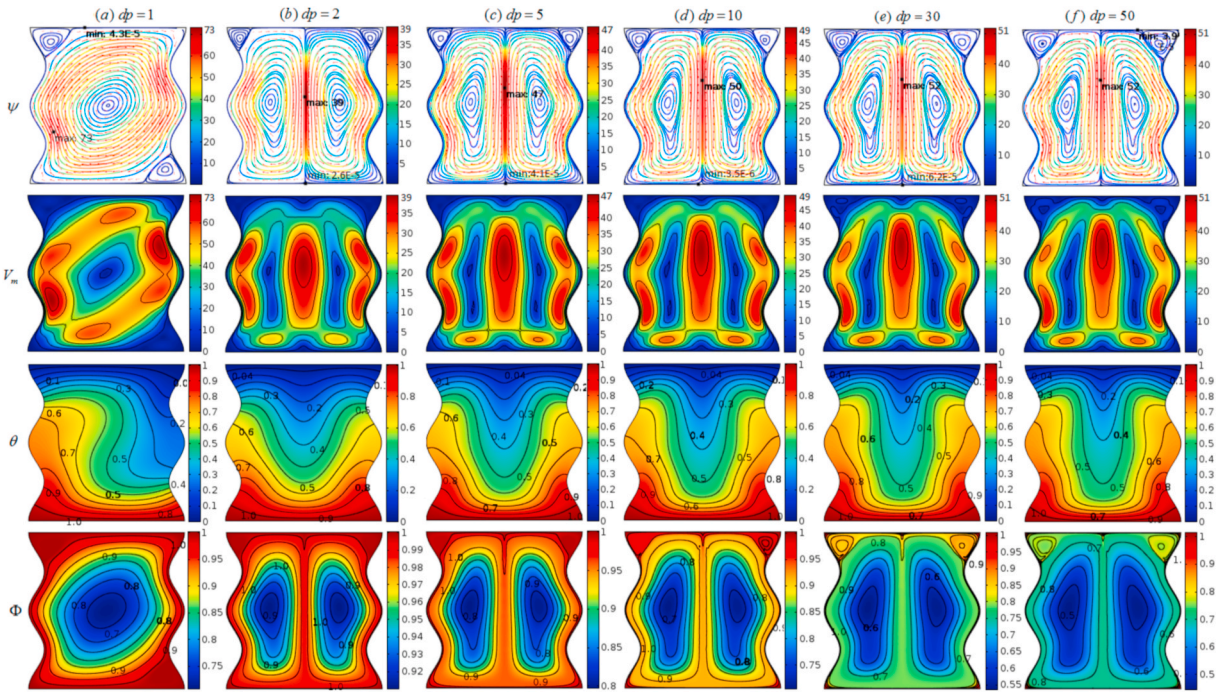

Fig. 15. The effects of the particle diameter (dp) effects for $\varphi = 0.025$, $Ha = 40$ $Ra_T = 5 \times 10^5$, $\chi = 0^o$ at $\tau = 2$.

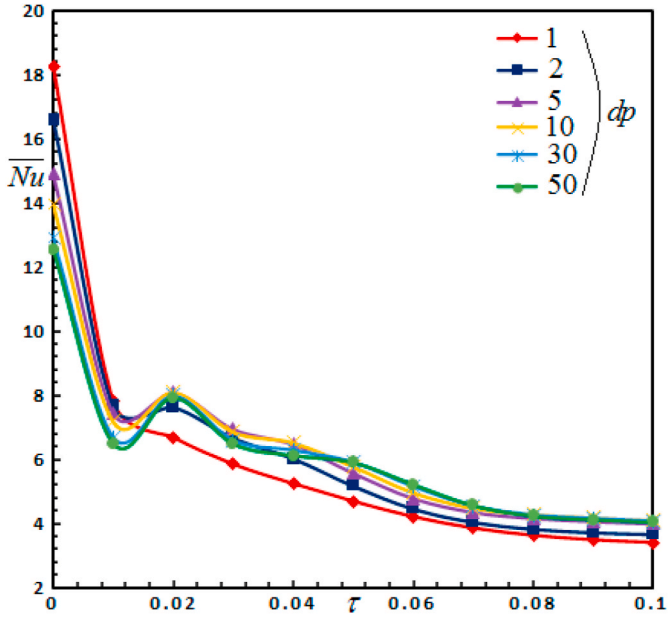

Fig. 16. Average Nusselt number with respect to time and nanoparticles diameter (dp) when $Ra_T = 2.3 \times 10^5$, $\varphi = 0.025$, $Ha = 40$, $\chi = 0^o$.

transfer rate is higher for all cases which subsides vividly at $\tau = 0.01$ and then fluctuates and decreases before it becomes steady. When the nanoparticles diameter is between 10 and 50 nm, it takes less time for the heat transport rate to become stable then the particle diameter 1–5 nm. Specifically, when the diameter of the nanoparticles increased from 1 nm to 10 nm, the average heat transfer decreased by 16.74%, but when the diameter of the nanoparticles increased from 10 nm to 50 nm, the average heat transfer did not change much. The heat transfer rate is almost the same for all species larger than 50 nm. This means that if the particle size is less than 50 nm, a large amount of flow operation can be observed. This happens because the smaller-sized copper oxide nanoparticles can be matched with the water molecules (0.3 nm) in the solution.

5. Conclusion

This article discusses the natural convective heat transport and the flow analysis of copper oxide-water nanofluid in a square vessel with two vertical curvy surfaces. The numerical experiment is conducted in the hydromagnetic flow field. The nonhomogeneous dynamic model is applied in the investigation. The results are analyzed from the physical and engineering perspective. The authors believe that the obtained results are purely applicable in the industry and innovative in the literature. However, for applying the obtained results to the industry, further examinations may be required. The main results are as follows:

(1) Nanofluids with an advanced volume fraction of nanoparticle exhibit lower stimuli in the flow and require higher buoyancy to obtain the maximum vitality flow. Higher flow configurations can be obtained in nanofluids with a lower nanoparticle volume fraction.
(2) The average heat transfer of the heat Rayleigh number from 10^3 to 10^4 remains stable. Whenever it increases to 10^6, the mean heat transfer improves by 158.70%.
(3) The non-wave vertical surface of the container has a higher heat transference rate. When the wave number is increased to 2, the heat transmission is reduced by 16.98%, and when the wave number is amplified from 2 to 4, the heat transference is increased by 3.62%.
(4) If the inclination of the magnetic field changes from 0° to 60°, the average heat transfer increases by 148.85%. However, if the inclination angle of the magnetic field is 60°, a stable maximum average heat transfer occurs.
(5) The average heat transfer declines by 64.08% if the value of the Hartmann number changes from 0 to 40.
(6) When the diameter of the nanoparticle upsurges from 1 nm to 10 nm, the average heat transfer reductions by 16.74%, but when the particle diameter increases from 10 nm to 50 nm, the average heat transfer decreases by 1.36%.

Credit author statement

M. J. Uddin: Conceptualization, Methodology, Software, Data curation, Writing – original draft, Visualization, Investigation, Supervision, Validation, Writing, Reviewing and Editing. S. K. Rasel: Software, Data curation, Writing – original draft, Visualization, Investigation, Validation, Writing, Reviewing and Editing. Jimoh K. Adewole: Visualization, Investigation, Validation, Writing, Reviewing and Editing. Khamis S. Al Kalbani: Visualization, Investigation, Validation, Writing, Reviewing and Editing

Declaration of competing interest

The authors state that there is no conflict of interest.

Acknowledgement

We would like to thank the anonymous referees for their constructive comments for further development of the paper. M. J. Uddin is thankful to the International Maritime College Oman, Sultanate of Oman for the research support through the grant 2022/CRG/11.

References

[1] A.B. Çolak, O. Yıldız, M. Bayrak, B.S. Tezekici, Experimental study for predicting the specific heat of water based Cu-Al2O3 hybrid nanofluid using artificial neural network and proposing new correlation, Int. J. Energy Res. 44 (9) (2020) 7198–7215.
[2] A.B. Çolak, O. Yildiz, M. Bayrak, A. Celen, S. Wongwises, Experimental study on the specific heat capacity measurement of water-based al2o3-cu hybrid nanofluid by using differential thermal analysis method, Curr. Nanosci. 16 (6) (2020) 912–928.
[3] M.J. Uddin, M.M. Rahman, Thermal instability analysis for natural convective heat transport within a horizontal layer filled with nanoparticles using non-homogeneous dynamic model, J. Eng. Thermophys. 30 (3) (2021) 476–493.
[4] M. Rahimi-Gorji, et al., Intraperitoneal Aerosolized drug delivery: technology, recent developments, and future outlook, Adv. Drug Deliv. Rev. (2020).
[5] H. Braet, et al., Exploring high pressure nebulization of Pluronic F127 hydrogels for intraperitoneal drug delivery, Eur. J. Pharm. Biopharm. 169 (2021) 134–143.
[6] M. Arifuzzaman, M.J. Uddin, Convective flow of alumina–water nanofluid in a square vessel in presence of the exothermic chemical reaction and hydromagnetic field, Results Eng. 10 (2021), 100226.
[7] K.S. Tshivhi, O.D. Makinde, "Magneto-nanofluid coolants past heated shrinking/stretching surfaces: dual solutions and stability analysis,", Results Eng. (2021), 100229.
[8] I.D.S. Maria, M.W. Lim, E. Von Lau, Multiple roles of graphene nanoparticles (GNP) in microbubble flotation for crude oil recovery from sand, Results Eng. 11 (2021), 100271.
[9] M.J. Uddin, M.M. Rahman, S. Alam, Fundamentals of nanofluids : evolution , applications and new theory, Int. J. Biomath. Syst. Biol. 2 (1) (2016) 1–31.
[10] D. Wen, G. Lin, S. Vafaei, K. Zhang, Review of nanofluids for heat transfer applications, Particuology 7 (2) (2009) 141–150.
[11] E. Abu-Nada, H.F. Oztop, Numerical analysis of Al2o3/Water nanofluids natural convection in a wavy walled cavity, Numer. Heat Transf. Part A Appl. 59 (5) (2011) 403–419.
[12] E. Abu-Nada, Z. Masoud, H.F. Oztop, A. Campo, Effect of nanofluid variable properties on natural convection in enclosures, Int. J. Therm. Sci. 49 (3) (2010) 479–491.
[13] D.S. Cimpean, C. Revnic, I. Pop, "Natural convection in a square inclined cavity filled with a porous medium with sinusoidal temperature distribution on both side walls,", Transport Porous Media 130 (2) (2019) 391–404.
[14] D.D. Vo, J. Alsarraf, A. Moradikazerouni, M. Afrand, H. Salehipour, C. Qi, Numerical investigation of γ-AlOOH nano-fluid convection performance in a wavy channel considering various shapes of nanoadditives, Powder Technol. 345 (2019) 649–657.
[15] C.-C. Cho, C.-L. Chen, Mixed convection heat transfer performance of water-based nanofluids in lid-driven cavity with wavy surfaces, Int. J. Therm. Sci. 68 (2013) 181–190.
[16] M. Nikfar, M. Mahmoodi, Meshless local Petrov–Galerkin analysis of free convection of nanofluid in a cavity with wavy side walls, Eng. Anal. Bound. Elem. 36 (3) (2012) 433–445.
[17] C.-C. Cho, Heat transfer and entropy generation of natural convection in nanofluid-filled square cavity with partially-heated wavy surface, Int. J. Heat Mass Tran. 77 (2014) 818–827.
[18] A.I. Alsabery, R. Mohebbi, A.J. Chamkha, I. Hashim, Effect of local thermal non-equilibrium model on natural convection in a nanofluid-filled wavy-walled porous cavity containing inner solid cylinder, Chem. Eng. Sci. 201 (2019) 247–263.
[19] W. Tang, M. Hatami, J. Zhou, D. Jing, Natural convection heat transfer in a nanofluid-filled cavity with double sinusoidal wavy walls of various phase deviations, Int. J. Heat Mass Tran. 115 (2017) 430–440.
[20] A. Abdulkadhim, H.K. Hamzah, F.H. Ali, A.M. Abed, I.M. Abed, Natural convection among inner corrugated cylinders inside wavy enclosure filled with nanofluid superposed in porous–nanofluid layers, Int. Commun. Heat Mass Tran. 109 (2019), 104350.
[21] K.M. Shirvan, R. Ellahi, M. Mamourian, M. Moghiman, Effects of wavy surface characteristics on natural convection heat transfer in a cosine corrugated square cavity filled with nanofluid, Int. J. Heat Mass Tran. 107 (2017) 1110–1118.
[22] R.Y. Emami, M. Siavashi, G.S. Moghaddam, The effect of inclination angle and hot wall configuration on Cu-water nanofluid natural convection inside a porous square cavity, Adv. Powder Technol. 29 (3) (2018) 519–536.
[23] M.A. Sheremet, T. Grosan, I. Pop, Natural convection and entropy generation in a square cavity with variable temperature side walls filled with a nanofluid: buongiorno's mathematical model, Entropy 19 (7) (2017) 337.
[24] M.A. Sheremet, D.S. Cimpean, I. Pop, Free convection in a partially heated wavy porous cavity filled with a nanofluid under the effects of Brownian diffusion and thermophoresis, Appl. Therm. Eng. 113 (2017) 413–418.
[25] N. Chandra Roy, Flow and heat transfer characteristics of a nanofluid between a square enclosure and a wavy wall obstacle, Phys. Fluids 31 (8) (2019), 82005.
[26] A.S. Dogonchi, M. Waqas, D.D. Ganji, Shape effects of Copper-Oxide (CuO) nanoparticles to determine the heat transfer filled in a partially heated rhombus enclosure: CVFEM approach, Int. Commun. Heat Mass Tran. 107 (2019) 14–23.
[27] A.R. Gheynani, et al., Investigating the effect of nanoparticles diameter on turbulent flow and heat transfer properties of non-Newtonian carboxymethyl cellulose/CuO fluid in a microtube, Int. J. Numer. Methods Heat Fluid Flow 29 (5) (2019) 1699–1723, https://doi.org/10.1108/HFF-07-2018-0368.
[28] N. Ullah, S. Nadeem, A.U. Khan, Finite element simulations for natural convective flow of nanofluid in a rectangular cavity having corrugated heated rods, J. Therm. Anal. Calorim. (2020) 1–13.
[29] A.P. Patel, D. Bhatnagar, S. Prabhu, Numerical study on turbulent natural convection and radiation heat transfer of nanofluids in a differentially heated square enclosure, J. Therm. Anal. Calorim. (2020) 1–10.
[30] Z. Abdelmalek, T. Tayebi, A.S. Dogonchi, A.J. Chamkha, D.D. Ganji, I. Tlili, Role of various configurations of a wavy circular heater on convective heat transfer within an enclosure filled with nanofluid, Int. Commun. Heat Mass Tran. 113 (2020), 104525.
[31] M.J. Uddin, S.K. Rasel, M.M. Rahman, K. Vajravelu, Natural convective heat transfer in a nanofluid-filled square vessel having a wavy upper surface in the presence of a magnetic field, Therm. Sci. Eng. Prog. 19 (2020), 100660.
[32] M.J. Uddin, A.K.M.F. Hoque, M.M. Rahman, K. Vajravelu, Numerical simulation of convective heat transport within the nanofluid filled vertical tube of plain and uneven side walls, Int. J. Thermofluid Sci. Technol. 6 (1) (2019), 19060101.
[33] M. Sheikholeslami, M. Gorji-Bandpy, D.D. Ganji, S. Soleimani, Effect of a magnetic field on natural convection in an inclined half-annulus enclosure filled with Cu–water nanofluid using CVFEM, Adv. Powder Technol. 24 (6) (2013) 980–991.
[34] R.K. Tiwari, M.K. Das, Heat transfer augmentation in a two-sided lid-driven differentially heated square cavity utilizing nanofluids, Int. J. Heat Mass Tran. 50 (9–10) (2007) 2002–2018.
[35] M.M. Rahman, S. Mojumder, S. Saha, S. Mekhilef, R. Saidur, Effect of solid volume fraction and tilt angle in a quarter circular solar thermal collectors filled with CNT–water nanofluid, Int. Commun. Heat Mass Tran. 57 (2014) 79–90.
[36] K. Khanafer, K. Vafai, M. Lightstone, Buoyancy-driven heat transfer enhancement in a two-dimensional enclosure utilizing nanofluids, Int. J. Heat Mass Tran. 46 (19) (2003) 3639–3653.
[37] Y. Xuan, Q. Li, W. Hu, Aggregation structure and thermal conductivity of nanofluids, AIChE J. 49 (4) (2003) 1038–1043.
[38] M.J. Uddin, M.M. Rahman, Heat transportation in copper oxide-water nanofluid filled triangular cavities, Int. J. Heat and Technology 38 (1) (2020) 106–124.
[39] M.J. Uddin, M.M. Rahman, Numerical computation of natural convective heat transport within nanofluids filled semi-circular shaped enclosure using nonhomogeneous dynamic model, Therm. Sci. Eng. Prog. 1 (2017) 25–38.
[40] J. Buongiorno, Convective transport in Nanofluids, 2006.
[41] O.C. Zienkiewicz, R.L. Taylor, R.L. Taylor, R.L. Taylor, The Finite Element Method: Solid Mechanics, vol. 2, Butterworth-heinemann, 2000.
[42] R. Codina, Comparison of some finite element methods for solving the diffusion-convection-reaction equation, Comput. Methods Appl. Mech. Eng. 156 (1–4) (1998) 185–210.
[43] M.J. Uddin, M.M. Rahman, Finite element computational procedure for convective flow of nanofluids in an annulus, Therm. Sci. Eng. Prog. 6 (2018) 251–267.
[44] B. Ghasemi, S.M. Aminossadati, Natural convection heat transfer in an inclined enclosure filled with a water-CuO nanofluid, Numer. Heat Transf. Part A Appl. 55 (8) (2009) 807–823.
[45] G. de Vahl Davis, Natural convection of air in a square cavity: a bench mark numerical solution, Int. J. Numer. Methods Fluid. 3 (3) (1983) 249–264.
[46] Z. Wan, J. Deng, B. Li, Y. Xu, X. Wang, Y. Tang, Thermal performance of a miniature loop heat pipe using water–copper nanofluid, Appl. Therm. Eng. 78 (2015) 712–719.

Nomenclature

a: reference wave amplitude (m)
$\overline{B}$: reference uniform magnetic field

B_o: magnitude of the uniform magnetic intensity (kg $s^{-2}A^{-1}$)
c_p: specific heat coefficient (J $kg^{-1}K^{-1}$)
C: nanofluid concentration (mol m^{-3})
C_C: nanofluid reference concentration without heating (mol m^{-3})
C_h: nanofluid reference concentration while heating (mol m^{-3})
d_p: nanoparticle diameter (nm)
D_B: Brownian diffusion coefficient (m^2s^{-1})
D_T: thermophoretic diffusion coefficient (m^2s^{-1})
$D_T^{'}$: numeric value of $\sqrt{D_T}$
$\overline{E}$: reference electric field
g: gravity force (ms^{-2})
Ha: Hartmann number
$\overline{J}_E$: Lorentz Force
k: reference wavy troughs
k_B: Boltzmann constant (JK^{-1})
L: reference length of the geometry (m)
Le: modified Lewis number
n: particles shape factor
Nu_L: local Nusselt number
$\overline{Nu}$: mean Nusselt number
N_{TB}: dynamic thermo-diffusion parameter
p: reference pressure (Pa)
P: dimensionless modified pressure
Pr: Prandtl number
Ra_C: local solute Rayleigh number
Ra_T: local heat Rayleigh number
Sc: Schmidt number
t: reference time
T: nanofluid temperature (K)
T_C: reference cold wall temperature (K)
T_h: reference hot wall temperature (K)
$(\overline{u}, \overline{v})$: velocity of nanofluid (ms^{-1})
(U, V): dimensionless nanofluid velocity components
V_m: average velocity magnitude of the flow
V_T: thermophoretic velocity equation (ms^{-1})
(x,y): reference coordinates
(X, Y): dimensionless coordinates

Greek Symbols

α: thermal diffusivity (m^2s^{-1})
β: coefficient of thermal expansion (K^{-1})
β^*: mass development coefficient (mol^{-1})
γ: reference angle between the magnetic field direction and the x-axis
$\Delta T = T_h - T_C$: reference temperature differences (K)
$\Delta C = C_h - C_C$: reference Concentration differences (mol m^{-3})
κ: thermal conductivity ($Wm^{-1}K^{-1}$)
μ: viscosity (kg $m^{-1}s^{-1}$)
σ: electrical conductivity
$\hbar$: correction factor
ρ: density(kgm^{-3})
φ: nanoparticle's volume fraction
Φ: dimensionless concentration
Ψ: sphericity
ψ: stream function
θ: dimension free temperature
τ: dimensionless time
χ: dimensionless angle between the magnetic field direction and the x-axis
ν_{bf}: kinematic viscosity of base fluid (m^2s^{-1})
ρc_p: volumetric heat capacity
$\rho\beta$: volumetric thermal expansion
$\rho\beta^*$: volumetric mass expansion nanoparticles

Suffixes

p: nanoparticles
bf: base-fluid
nf: nanofluid